PCCP

ROYAL SOCIETY OF CHEMISTRY

PAPER

View Article Online
View Journal | View Issue

Cite this: *Phys. Chem. Chem. Phys.*, 2023, **25**, 3867

Nanoscale domain imaging of Li-rich disordered rocksalt-type cathode materials with X-ray spectroscopic ptychography†

Hideshi Uematsu,[abc] Nozomu Ishiguro,[acd] Masaki Abe,[abc] Shuntaro Takazawa,[abc] Jungmin Kang,[c] Itsuki Konuma,[e] Naoaki Yabuuchi[e] and Yukio Takahashi[acdf]

Received 5th September 2022,
Accepted 9th January 2023

DOI: 10.1039/d2cp04087e

rsc.li/pccp

Lithium-rich disordered rocksalt-type cathode materials are promising for high-capacity and high-power lithium-ion batteries. Many of them are synthesized by mechanical milling and may have heterogeneous structures and chemical states at the nanoscale. In this study, we performed X-ray spectroscopic ptychography measurements of Li-rich disordered rocksalt-type oxide particles synthesized by mechanical milling before and after delithiation reaction at the vanadium K absorption edge, and visualized their structures and chemical state with a spatial resolution of ~100 nm. We classified multiple domains with different chemical states *via* clustering analysis. A comparison of the domain distribution trends of the particles before and after the delithiation reaction revealed the presence of domains, suggesting that the delithiation reaction was suppressed.

1 Introduction

Lithium-ion batteries have become indispensable in our society for use in mobile devices, automobiles, and even for storing surplus electricity. Cathode active materials with high energy density and fast charge/discharge capability are required. Li-rich metastable cathode materials have recently been attracting attention for the development of the cathode materials that satisfy the requirements. In Li-rich disordered rocksalt (DRS)-type cathode materials ($Li_xTM_{2-x}O_2$, $x > 1.1$ TM: transition metal elements; *e.g.*, V, Ti, Mn, Nb, Cr, Mo), Li and TM randomly occupy the same site.[1–7] They achieve a higher reversible capacity than conventional layered rocksalt type cathode active materials such as commercial $LiCoO_2$ and Li–Ni–Mn–Co–O_2 compounds.[1] Although such Li-rich DRS-type phases are often difficult to synthesize because of the need for sintering at high temperatures, they are synthesized by mechanical milling (MM).[1,8] MM is a simple and powerful approach to obtaining metastable, amorphous, nanocomposite, and nanosized particles by mixing and crushing powders.[9] It is expected that the reversible capacity and rate capability can be increased by reducing the particle size to the nanoscale by MM.[4] Note that MM is a physical mixing process; hence, there are chemical and structural heterogeneities in the synthesized materials. Chemical and structural heterogeneities will consequently lead to a heterogeneous de-/lithiation reaction distribution, where reactions proceed only in a certain domain. Moreover, such a de-/lithiation reaction distribution will cause the capacity fade with local overcharge/overdischarge and structural degradation.[10–13] Therefore, it is crucial to observe the heterogeneous structures at the nanoscale and identify the domains where the de-/lithiation reaction proceeds.

X-ray spectroscopic microscopy using synchrotron radiation has been extensively used to visualize heterogeneous structures in bulk materials.[14,15] In particular, X-ray spectroscopic ptychography[16] is a promising tool for obtaining spatially resolved X-ray absorption fine structure (XAFS) spectra and phase

[a] *International Center for Synchrotron Radiation Innovation Smart (SRIS), Tohoku University, 2-1-1 Katahira, Aoba-ku, Sendai 980-8577, Japan. E-mail: hideshi.uematsu.r5@dc.tohoku.ac.jp, nozomu.ishiguro.c1@tohoku.ac.jp, ytakahashi@tohoku.ac.jp*
[b] *Department of Metallurgy, Materials Science and Materials Processing, Graduate School of Engineering, Tohoku University6-6-2 Aoba-yama, Aoba-ku, Sendai 980-8579, Japan*
[c] *RIKEN SPring-8 Center, 1-1-1, Koto, Sayo, Hyogo 679-5148, Japan*
[d] *Institute of Multidisciplinary Research for Advanced Materials (IMRAM), Tohoku University, 2-1-1 Katahira, Aoba-ku, Sendai 980-8577, Japan*
[e] *Department of Chemistry and Life Science, Yokohama National University, 79-5 Tokiwadai, Hodogaya-ku Yokohama, Kanagawa, 240-8501, Japan*
[f] *Institute for Materials Research, Tohoku University, 2-1-1 Katahira, Aoba-ku, Sendai, Miyagi 980-8577, Japan*

† Electronic supplementary information (ESI) available: Sample synthesis, electrochemical analysis, XRD and conventional XAFS of powder samples, spatial-resolution analysis of reconstructed images and chemical state maps of standard samples, histogram of chemical state maps, within-cluster sum of squared errors against the number of clusters, and average values and the probability density maps of chemical state maps in each cluster. See DOI: **https://doi.org/10.1039/d2cp04087e**

images with a spatial resolution of 40–80 nm, independent of lens fabrication accuracy. Chemical state imagings of the gold nanoparticles,[17] lithium iron phosphate cathode,[18,19] Pt-supported ceria–zirconia (CZ) solid-solution catalyst,[20,21] and zinc-oxide coated nanoporous alumina[22] have been performed by analyzing spatially resolved XAFS spectra obtained by X-ray spectroscopic ptychography. In addition, X-ray spectroscopic ptychography measurements have been applied in the determination of crystal orientation in polycrystalline vanadium oxide using the linear polarization dependency of XAFS[23] and the local coordination structure in manganese oxide in a nanoscale area using an extended X-ray absorption fine structure.[24] X-ray spectroscopic microscopy measurements provide spatially resolved chemical state information from image data with more than 10^3 pixels. Machine learning methods can help reconstruct such huge complex data into lower-dimensional data that is easier for humans to understand. Machine learning methods are expected to mine hidden material information and promote better materials design. Thus, the detection of inert domains in $LiCoO_2$ particles on electrodes,[25] the analysis of oxygen diffusion pathways in CZ particles,[20] and the classification of Ni K-edge XAFS spectra of Ni-rich cathode active material particles[26] have been reported. Recently, we have reported the presence of multiple domains in spinel-type lithium nickel manganese oxide cathode particle by analyzing the correlation between the valence and the composition.[27] The combination of X-ray spectroscopic ptychography and machine learning is expected to enable the visualization of nanoscale domains.

In this study, we selected $_{0.25}Li_2O^{-}{}_{0.75}LiVO_2$ ($Li_{10/7}V_{6/7}O_2$) particles as an example of Li-rich DRS-type cathode material synthesized by MM. X-ray spectroscopic ptychography measurements were performed at the vanadium (V) K edge. The chemical state maps reflecting the V valence, the V site symmetry, and the composition were derived from the spatially resolved X-ray absorption near-edge structure (XANES) and phase images. Moreover, we visualized the domains with different chemical states by clustering analysis.

2 Experimental

2.1 Sample preparation

$Li_{10/7}V_{6/7}O_2$, which is a solid solution sample, $x = 0.25$ in $xLi_2O-(1-x)LiVO_2$, was synthesized by MM (denoted as as-prepared $Li_{10/7}V_{6/7}O_2$). The details of the synthesis processes are presented in ESI.† To simulate the half charged state of $Li_{10/7}V_{6/7}O_2$, chemical delithiation was performed on as-prepared $Li_{10/7}V_{6/7}O_2$ using iodine in acetonitrile (denoted as delithiated $Li_{10/7}V_{6/7}O_2$). We prepared $LiVO_2$ (ESI†) and $LiVO_3$ (ESI†) as standard compounds in spectroscopic ptychogrpahy. X-ray diffraction (XRD) patterns of as-prepared $Li_{10/7}V_{6/7}O_2$ (Fig. S1, ESI†) showed peaks corresponding to those of $Fm\bar{3}m$ space groups, but no peaks corresponding to those of layered rocksalt-type $LiVO_2$ (space group $R\bar{3}m$) are found. The reversible capacity of the $Li_{10/7}V_{6/7}O_2$ electrode reaches > 350 mA h g^{-1} with good capacity retention (Fig. S2, ESI†). This capacity was superior to that of nanosized $Li_{1.2}V_{0.6}Nb_{0.2}O_2$ synthesized by MM[6] and that of Li_3PO_4, where Li atoms occupy tetrahedral sites as in Li_2O, integrated into $LiMnO_2$.[28]

2.2 X-ray spectroscopic ptychography

The as-prepared $Li_{10/7}V_{6/7}O_2$, delithiated $Li_{10/7}V_{6/7}O_2$, $LiVO_2$, and $LiVO_3$ particles were dispersed in respective acetonitrile solutions, dropped on respective 500 nm-thick Si_3N_4 membranes (Norcada) in argon atmosphere glove box, and kept in an argon atmosphere until mounting on the piezoelectric stage inside the ptychography chamber in vacuum. X-ray spectroscopic ptychography experiments were performed at the BL29XUL beamline of SPring-8. The incident X-ray was monochromatized by the Si(111) double-crystal monochromator and focused using Kirzpatrick–Baez mirrors to a size of 300 nm (FHWM). Forty X-ray energies between 5420 and 5540 eV were selected with the smallest energy gap of 0.5 eV. The samples were placed in the focal plane and raster-scanned with a step width of 150 nm. The exposure time at each position was 1 s. Multiple diffraction patterns were collected using a pixel array detector (Dectris EIGER 1 M). The measurement of all energy points took 4–8 h per particle. Probe and projected sample images were reconstructed by an extended ptychographic iterative engine[29] with the Kramers–Kronig relationship (KKR) constraint.[30] The input of initial images of the sample were unity, and those of the probe were calculated on the basis of the experimental setup. Iterative calculations were performed for 800 cycles, and the KKR constraint was applied every 50 cycles after the 500th iteration.

2.3 Curve-fitting analysis for spatially resolved XANES

To evaluate features of the spatially resolved XANES, such as the height of the edge jump and the height and width of the pre-edge peak, the curve-fitting analysis of V K-edge XANES was performed on each pixel using

$$\mu t_{\mathrm{fit}}(E) = a + \frac{b_1}{2}\left\{1 + \mathrm{erf}\left(\frac{E-b_2}{b_3}\right)\right\} + \sum_{i=1}^{2}\frac{c_{i1}}{1+\left(\frac{E-c_{i2}}{c_{i3}}\right)^2}, \quad (1)$$

where a, b_1, b_2, b_3, and c_{ij} are fitting parameters, and E is incident X-ray energy. The edge jump ($\equiv \Delta\mu t$), proportional to the amount of V atoms in the image pixel, is estimated as b_1, and the edge energy, depending on the V valence, is estimated as b_2. The pre-edge peak intensity, depending on the V site symmetry, is estimated from $\pi c_{11}c_{13}(\equiv \mathrm{PE})$, and the normalized peak intensity ($\mathrm{PE}/\Delta\mu t$) is estimated. Note that the noise level of the absorption signal (σ_{Noise}) is estimated on the basis of the standard deviation at the four points between 5420 and 5466 eV before the absorption edge. Pixels where $\Delta\mu t < \sigma_{\mathrm{Noise}}$ were regarded as the missing-data regions because curvefitting is not reasonable. Then, at each pixel, the projected V atom density N_{V} and the effective projected electron density $\mathrm{Re}[N_{\mathrm{e}}^{\mathrm{eff}}]$ are

estimated using $\Delta\mu t$ and phase shift $\phi(E)$, respectively, according to

$$N_V = \frac{\Delta\mu t}{r_e \lambda \Delta f_V''}, \quad (2)$$

$$\mathrm{Re}[N_e^{\mathrm{eff}}] = \sum_j N_j \left\{ Z_j + f_j'(E) \right\} = -\frac{\phi}{r_e \lambda}, \quad (3)$$

where N_j is the projected density of j (= Li, V, O) atoms, r_e is the Thomson scattering length, λ is the wavelength of the incident X-ray, f_j' and f_j'' are the real and imaginary parts of the anomalous dispersion term of the atomic scattering factor, respectively, and $\Delta f_V''$ is the difference between the f_V'' values before and after the edge jump. The values of $\Delta f_V''$ was estimated to be 3.53 from database references,[31] and f_{Li}', f_V', and f_O' are 0.00278, −7.14, and 0.0757, respectively. Then, $\mathrm{Re}[N_e^{\mathrm{eff}}]/N_V$ is given as

$$\frac{\mathrm{Re}[N_e^{\mathrm{eff}}]}{N_V} = \frac{\sum_j N_j \left\{ Z_j + f_j'(E) \right\}}{N_V} \quad (4)$$

$$= (23 + f_V') + \frac{(3 + f_{Li}')N_{Li} + (8 + f_O')N_O}{N_V}, \quad (5)$$

which depends on the (Li + O + V)/V molar ratio. The theoretical values of $\mathrm{Re}[N_e^{\mathrm{eff}}]/N_V$ for $Li_{10/7}V_{6/7}O_2$, $LiVO_2$, and $LiVO_3$ are estimated to be 39.7, 35.0, and 43.1, respectively.

2.4 Clustering analysis

We performed clustering analysis by the k-means method[32] based on the similarity between the pixels in three-dimensional data space with descriptors such as edge energy, PE/$\Delta\mu t$, and $\mathrm{Re}[N_e^{\mathrm{eff}}]/N_V$ for the data clustering. The number of clusters was set to 6, where the slope of the decrease in the within-cluster sum of squared error is gradual (Fig. S3, ESI†), as determined by the elbow method.[33]

3 Results and discussion

3.1 Reconstructed images and spatially resolved XANES

Fig. 1(a)–(c), respectively, show the field-emission scanning electron microscopy (SEM), reconstructed absorption, and reconstructed phase images of as-prepared $Li_{10/7}V_{6/7}O_2$ particles P1–P3 and delithiated $Li_{10/7}V_{6/7}O_2$ particles D1–D3. The pixel size of the reconstructed images is 15 nm. The absorption image at the energy above the V K-edge depends on the number of V atoms along the incident X-ray direction. On the other hand, the phase shift originates from the amount of electrons, which reflects the amount of all existing atoms, including the lighter Li and O. The full-period spatial resolutions of the reconstructed images were estimated to be better than 80–120 nm using the phase retrieval transfer function (Fig. S5, ESI†). The shape of the particles in the phase images (Fig. 1(c)) is in good agreement with that in the SEM images (Fig. 1(a)).

By stacking the reconstructed absorption and phase images, spatially resolved V K-edge XANES and phase spectra were successfully obtained, as shown in Fig. 1(d) and (e). The spatially resolved XANES spectra are in good agreement with the conventional XAFS spectra (Fig. S4, ESI†) of the pellet sample, where the absorption edge energy and pre-edge peak intensity were increased in delithiated $Li_{10/7}V_{6/7}O_2$ compared with those in as-prepared $Li_{10/7}V_{6/7}O_2$. Chaurand *et al.* have reported that the V K-edge energy increases with the V valence.[34] The shift of the absorption edge should reflect the valence change with delithiation (ESI† Fig. S4). As shown in Fig. 1(d), the edge energy differed between particles, and there

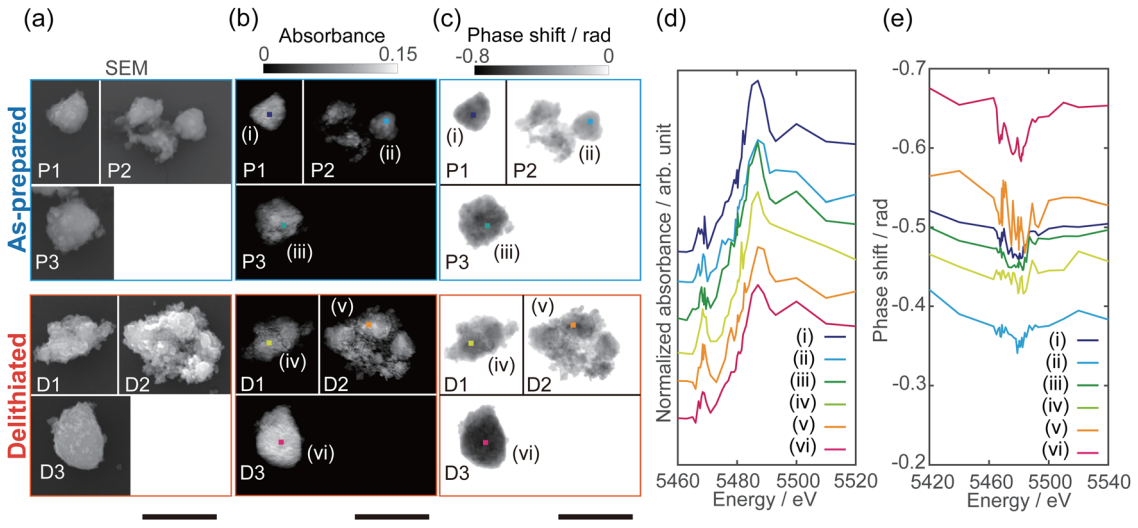

Fig. 1 (a–c) Images of as-prepared $Li_{10/7}V_{6/7}O_2$ particles P1–P3 and delithiated $Li_{10/7}V_{6/7}O_2$ particles D1–D3. (a) SEM images. (b) Reconstructed absorption images at 5540 eV. (c) Reconstructed phase shift images at 5420 eV. The pixel size of reconstructed images is 15 nm. The scale bars are 2 μm. (d) XANES and (e) phase spectra of as-prepared and delithiated $Li_{10/7}V_{6/7}O_2$ particles. Offset is added to the V K-edge XANES spectra in (d). The extracted size of both spectra (d and e) is 120 × 120 nm^2.

are regions that do not follow the trend of the edge energy in the conventional XAFS spectra.

The characteristic peak around 5466 eV, known as the pre-edge peak, is related to the electronic transition of the 1s electron to 3d orbitals in compounds of 3d-transition metals such as V, Mn, and Ti. The pre-edge peak intensity indicates the degree of d–p hybridization, allowing forbidden 1s → 3d transition; the degree of hybridization of 4p orbitals or ligand 2p orbitals with the 3d orbitals depends on the site symmetry (*i.e.*, coordination structure).[35,36] Chaurand *et al.* have reported that the pre-edge peak intensities in the V K-edge XANES spectra increase in the order of the tetrahedral structure (Na_3VO_4), the pyramidal structure (V_2O_5), and the octahedral structure ($Ca_3(V_{10}O_{28})-17H_2O$).[34] Nakajima *et al.* have proposed that the V atoms in the DRS-type Li–Nb–V–O_2 cathode material reversibly migrate from octahedral to tetrahedral sites during charging, on the basis of the result of the operando XAFS measurement.[2] In addition, Baur *et al.* have reported that formation of tetrahedrally coordinated V in the amorphous phase from the DRS-type Li_2VO_2F cathode during charging, based on the X-ray total scattering data.[3] As shown in Fig. 1(d), the pre-edge peak intensities in the delithiated $Li_{10/7}V_{6/7}O_2$ particles increase compared with those in the as-prepared $Li_{10/7}V_{6/7}O_2$ particles, indicating an increase in the V valence and/or the amount of tetrahedrally coordinated V.

3.2 Chemical state mapping

Chemical state mapping was performed by the curve-fitting analysis of spatially resolved XANES spectra and the phase images. We succeeded in extracting the following three chemical state maps: edge energy, $Re[N_e^{eff}]/N_V$, and normalized pre-edge peak intensity ($PE/\Delta\mu t$), which depend on the V valence, (Li + V + O)/V molar ratio, and V site symmetry, respectively. Fig. 2(a)–(c) show the derived chemical state maps of as-prepared and delithiated $Li_{10/7}V_{6/7}O_2$ particles. ESI† S6 show the reconstructed images of $LiVO_2$ and $LiVO_3$, and their spatially resolved XANES and phase spectra. Fig. S7 (ESI†) show the chemical state maps of $LiVO_2$ and $LiVO_3$. As shown in Fig. 2(a)–(c), there are a gradient from the surface and a mottled appearance at the submicron order such as heterogeneous distributions, while such distributions are not observed in the chemical state maps in $LiVO_2$ and $LiVO_3$. The heterogeneous distributions within each as-prepared $Li_{10/7}V_{6/7}O_2$ particle and within each delithiated $Li_{10/7}V_{6/7}O_2$ particle are also seen in the histograms of chemical state maps for all measured particles (see ESI† S8).

Now, we discuss the heterogeneous distribution of chemical state maps at the particle level. As shown in the enlarged view of the as-prepared $Li_{10/7}V_{6/7}O_2$ particle P2 in Fig. 2(a), the V valence increases from the bulk to the surface of the particle toward V^{5+}, suggesting that oxidation occurs from the surface to the bulk during synthesis. As for the delithiated $Li_{10/7}V_{6/7}O_2$ particles, there were some regions remaining V^{3+}, especially at the particle D1, even after the chemical delithiation. In the enlarged view of the delithiated $Li_{10/7}V_{6/7}O_2$ particle D1 shown in Fig. 2(a), the region close to V^{5+} is localized, indicating that the delithiation reaction is inhibited within the particle and that the particle D1 has a lower delithiation reactivity than the other particles. As shown in Fig. 2(b), a mottled appearance is observed in $Re[N_e^{eff}]/N_V$ maps for the as-prepared $Li_{10/7}V_{6/7}O_2$ particle P3 and also the delithiated $Li_{10/7}V_{6/7}O_2$ particle D2, indicating the heterogeneous distribution of Li- or O-rich

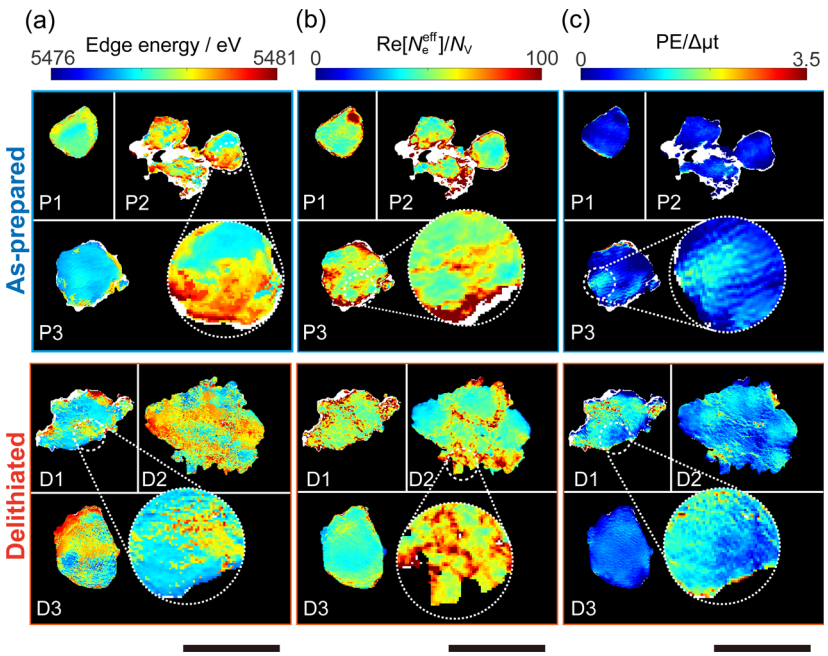

Fig. 2 Chemical state maps of as-prepared $Li_{10/7}V_{6/7}O_2$ particles P1–P3 and delithiated $Li_{10/7}V_{6/7}O_2$ particles D1–D3. (a) Edge energy. (b) $Re[N_e^{eff}]/N_V$ (c) $PE/\Delta\mu t$. The pixel size of chemical state maps is 15 nm. The scale bars are 2 μm. Values in white areas are missing because fitting was not possible.

phases such as Li_2O, implying that $LiVO_2$ and Li_2O were not completely mixed by MM. As shown in the enlarged image of the delithiated $Li_{10/7}V_{6/7}O_2$ particle D1 in Fig. 2(c), the high PE/$\Delta\mu$t region is distributed around the region close to V^{5+} shown in Fig. 2(a), which may be due to the relationship between the delithiation reaction and the V site symmetry. Lee *et al.* have proposed that Li moves in the DRS phase through the octahedral–tetrahedral–octahedral sites diffusion pathway on an atomic scale (percolation theory).[5] Taking into consideration this atomic-scale Li diffusion pathway, the V ions occupying tetrahedral sites are considered to be a barrier to Li diffusion. The distribution of PE/$\Delta\mu t$ in the surrounding region close to V^{5+} may reflect the inhibition of Li diffusion.

3.3 Nanoscale domain imaging using clustering analysis

Domains with different characteristics, such as regions where it is difficult/easy for the delithiation reaction and impurity phases to proceed are expected to have different correlations between the chemical states. We performed clustering (grouping) analysis based on the similarity of chemical states among edge energy, Re[N_e^{eff}]/N_V, and PE/$\Delta\mu t$, and grouped all pixels into 6 clusters. Fig. 3(a) shows the real-space distributions of 6 clusters, which are domain structures. We succeeded in visualizing domains with different correlations between V valence, composition, and V site symmetry. As far as we can see from Fig. 3(a), the domain sizes were estimated to be between 100–1000 nm. However, the images in Fig. 3(a) are generated projection images along incident X-rays (Fig. 2), and we cannot distinguish the overlapping domains. The domain structures are different between as-prepared and delithiated $Li_{10/7}V_{6/7}O_2$ particles. Cluster 1 is more abundant in the as-prepared $Li_{10/7}V_{6/7}O_2$ particles than in the delithiated $Li_{10/7}V_{6/7}O_2$ particles and is also observed in the delithiated $Li_{10/7}V_{6/7}O_2$ particle D1. Cluster 2 is partially observed in the as-prepared $Li_{10/7}V_{6/7}O_2$ particle P3 and is abundant in the delithiated $Li_{10/7}V_{6/7}O_2$ particle D1. Cluster 3 is distributed in delithiated $Li_{10/7}V_{6/7}O_2$ particles and is rarely observed in as-prepared $Li_{10/7}V_{6/7}O_2$ particles. Cluster 4 is observed around the surface of a particle, especially in the as-prepared $Li_{10/7}V_{6/7}O_2$ particle P2. Clusters 5 and 6 are less abundant than other cluster, and are distributed around the surface of a particle.

Fig. 3(b) shows the probability density distributions of the chemical states. The three-dimensional scattering plots and two-dimensional probability density are shown in ESI† Fig. S9. As mentioned in Section 3.1, the edge energy depends on the V valence and increases with the V valence. The high PE/$\Delta\mu t$ reflects a tetrahedral structure, and the low PE/$\Delta\mu t$ reflects an octahedral structure. The high Re[N_e^{eff}]/N_V reflects Li- and/or O-rich composition. In cluster 1, the V valence tends to be V^{3+} compared with those in clusters 3–5. Cluster 1 tends to be an octahedral structure and to be Li- and O-rich compared with clusters 3 and 4. In cluster 2, the V valence is close to V^{3+}, as in cluster 1, but cluster 2 tends to be a tetrahedral structure. Cluster 2 tends to be Li- and O-poor compared with clusters 3 and 4. In cluster 3, the V valence tends to be V^{5+}. Cluster 3 tends to be a tetrahedral structure. Cluster 3 is relatively Li- or O-poor compared with clusters 1 and 2. In cluster 4, the V valence tends to be V^{5+}. Cluster 4 tends to be an octahedral structure. Clusters 5 and 6 are mostly located at the outer edges of the particles, and Re[N_e^{eff}]/N_V values in clusters 5 and 6 are almost two times larger than those in clusters 1–4. The tendency of the

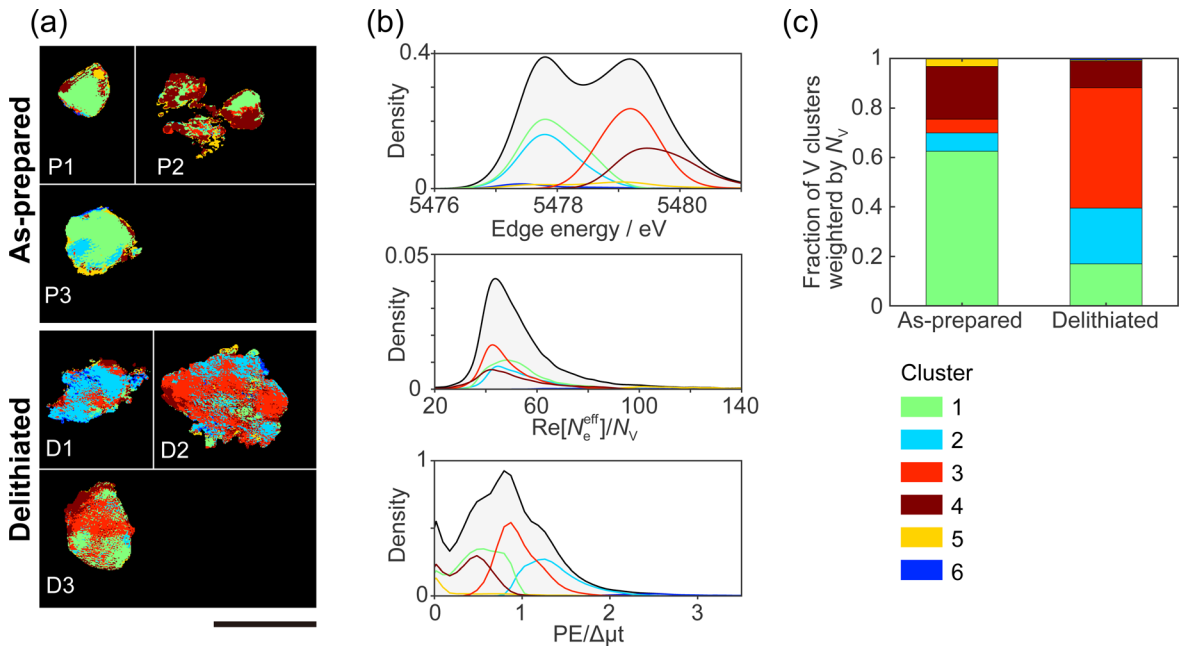

Fig. 3 Results of clustering analysis. (a) Spatial distribution of clusters 1–6. The scale bar is 2 μm. (b) Projected probability density distribution of (top) edge energy, (center) Re[N_e^{eff}]/N_V, and (bottom) PE/Dmt. (c) Fraction of clusters weighted by N_V in as-prepared and delithiated $Li_{10/7}V_{6/7}O_2$ particles. Each cluster is shown by the same color in (a), (b), and (c).

chemical states for each cluster is also seen in the XANES spectra averaged for each cluster (ESI† Fig. S9(e)).

Fig. 3(c) shows the fractions of the clusters in the as-prepared and delithiated $Li_{10/7}V_{6/7}O_2$ particles. The fractions of the clusters are weighted by N_V. Cluster 1 is predominant for the as-prepared $Li_{10/7}V_{6/7}O_2$ particles and a minority for the delithiated $Li_{10/7}V_{6/7}O_2$ particles. On the other hand, cluster 3 is a minority for the as-prepared $Li_{10/7}V_{6/7}O_2$ particles and predominant for the delithiated $Li_{10/7}V_{6/7}O_2$ particles. The reversal of the fraction of clusters 1 and 3 could be due to the change of cluster 1 into cluster 3 with delithiation. Konuma *et al.* have reported that octahedrally coordinated V^{3+} reversibly migrates to tetrahedrally coordinated V^{5+} during charge/discharging process in $Li_{8/7}Ti_{2/7}V_{4/7}O_2$ DRS-type cathode, and also the migration of V ion is related to the invariant volume in electrode.[7] The change in the fractions of cluster 1 and 3 can be related to the previous study. X-ray spectroscopic ptychography will provide information between macroscopic and atomic structures by visualizing the domain structure. The fraction of cluster 2 is higher in the delithiated $Li_{10/7}V_{6/7}O_2$ particles than in the as-prepared $Li_{10/7}V_{6/7}O_2$ particles. There are two possible origins of cluster 2. The first possibility is that the tetrahedral site is occupied by V^{3+} in the MM stage, and it remains without undergoing the delithiation reaction. This may be because V ions remain in the tetrahedral site when moving from one octahedral site to the neighboring octahedral site during the formation of the DRS-type structure in MM synthesis. The second possibility is that cluster 2 is generated from other clusters during reactions associated with the delithiation reaction, *e.g.*, disproportionation reaction,[37] *i.e.*, $2V^{4+} \rightarrow V^{3+} + V^{5+}$, and/or the structural changes to an amorphous phase.[3] Most charging and discharging are caused by a redox of V^{3+}/V^{5+}. Thus, cluster 2 that keeps V^{3+} in delithiated $Li_{10/7}V_{6/7}O_2$ particles will not contribute to the capacity during charging. The domain belonging to cluster 2 will become a barrier to Li diffusion. To improve the capacity and rate capability of cathode materials, it is important to avoid producing the domain belonging to cluster 2 during MM synthesis and charging/discharging processes, for example, doping additives such as Nb stabilizing the atomic framework of DRS phase[2] might be effective.

4 Conclusions

We have successfully visualized the chemical state distributions of the V valence, V site symmetry, and composition of Li-rich DRS-type vanadium oxide particles as synthesized by MM and their delithiated particles, using X-ray spectroscopic ptychography. The clustering analysis resulted in the division of chemical state maps into 6 clusters. The real-space distribution of the 6 clusters is the heterogeneous domain structure within and between particles, even in the synthesis stage. There were domains where the delithiation reaction proceeds or is inhibited in the particles. It is necessary for the delithiation reaction to occur in all particles to maximize the charge–discharge capacity.

In this study, the resolution of X-ray spectroscopic ptychography was ~100 nm. The spatial resolution depends mainly on the performance of the synchrotron source. We measured chemically delithiated particles to investigate the domain structure. Although the kinetics of electrochemical delithiation is expected to be more complex than that of chemical delithiation because of the presence of the other battery components, such as the electrolyte, binder, and conductive additives, the structural (thermodynamical) changes are by either electrochemical or chemical delithiation is considered similar.[38] Still, operando measurement under working or simulated conditions in the actual battery is required to investigate the proceeding of the delithiation reaction in the electrode. Furthermore, operando measurements coupling with the impedance method that provides electrical signals of surface degradation, cracks, *etc.*, will be helpful to investigate relationships between the impedance and microstructure changes. However, there are two large challenges to affording operando measurement. First is the improvement of the signal-to-noise ratio of spatially resolved XAFS spectra. The transmitted X-ray is attenuated to 1/10 in the 500 μm electrolyte at 5500 eV, and scattering from the electrolyte should also be considerable. Therefore, the total cell thickness, including the X-ray window, is preferably restrained to less than 50 μm. The second is measurement time. X-ray spectroscopic ptychography measurement takes 4–8 hours to obtain spatially resolved XANES region spectra of a μm size particle.[27] Thus, it can only visualize a stable or steady state of samples presently. Therefore it is necessary to shorten the measurement time to measure more dynamic aspects of electrochemical reactions in various conditions. To overcome the above challenges, low-emittance beam with higher brightness X-rays, high dynamic-range detector to capture high brightness X-rays, and sparse measurement to reduce energy points[39] are required. In the synchrotron radiation facilities with a low-emittance storage ring, which have been built or are under construction at several locations around the world, higher brightness will be provided. In the near future, we believe that X-ray spectroscopic ptychography will contribute to the design of functional materials with complex and heterogeneous structures at the nanoscale.

Author contributions

H. U.: conceptualization, methodology, software, investigation, visualization, writing – original draft preparation. N. I.: conceptualization, methodology, software, investigation, project administration, writing – reviewing and editing. M. A., S. T. and J. K. methodology, investigation. I. K.: investigation, resources, writing – reviewing and editing. N. Y.: resources, supervision, writing – reviewing and editing. Y. T.: conceptualization, methodology, project administration, writing – reviewing and editing.

Conflicts of interest

There are no conflicts to declare.

Acknowledgements

This work was supported by the Japan Society for the Promotion of Science (JSPS) KAKENHI (Grant No. JP18H05253, JP19H05814, JP20K15375, JP20K20523 and JP22J21779), Iketani Science and Technology Foundation (ISTF) (Grant No. 0331102-A), and Ministry of Education, Culture, Sports, Science and Technology of Japan (MEXT) program: ''Data Creation and Utilization-Type Material Research and Development'' project (Grant No. JPMXP1122712807). It was also supported in part by the ''Dynamic Alliance for Open Innovation Bridging Human, Environment and Materials'' project from the MEXT. The conventional transmission XAFS measurement was performed on BL37XU at SPring-8 with the approval of the Japan Synchrotron Radiation Research Institute (JASRI) (Proposal No. 2021A1483 and 2021B1566).

Notes and references

1 R. J. Clément, Z. Lun and G. Ceder, *Energy Environ. Sci.*, 2020, **13**, 345–373.
2 M. Nakajima and N. Yabuuchi, *Chem. Mater.*, 2017, **29**, 6927–6935.
3 C. Baur, C. Baur, M. E. Lăcătuşu, M. Fichtner, M. Fichtner and R. E. Johnsen, *ACS Appl. Mater. Interfaces*, 2020, **12**, 27010–27016.
4 N. Yabuuchi, *Curr. Opin. Electrochem.*, 2022, **34**, 100978.
5 J. Lee, A. Urban, X. Li, D. Su, G. Hautier and G. Ceder, *Science*, 2014, **343**, 519–522.
6 R. Qi, B. D. Campéon, I. Konuma, Y. Sato, Y. Kaneda, M. Kondo and N. Yabuuchi, *Electrochemistry*, 2022, **90**, 4–9.
7 I. Konuma, D. Goonetilleke, N. Sharma, T. Miyuki, S. Hiroi, K. Ohara, Y. Yamakawa, Y. Morino, H. B. Rajendra, T. Ishigaki and N. Yabuuchi, *Nat. Mater.*, 2022, DOI: 10.1038/s41563-022-01421-z.
8 J. Chable, C. Baur, J. H. Chang, S. Wenzel, J. M. García-Lastra and T. Vegge, *J. Phys. Chem. C*, 2020, **124**, 2229–2237.
9 T. Prasad Yadav, R. Manohar Yadav and D. Pratap Singh, *Nanosci. Nanotechnol.*, 2012, **2**, 22–48.
10 J. Liu, M. Kunz, K. Chen, N. Tamura and T. J. Richardson, *J. Phys. Chem. Lett.*, 2010, **1**, 2120–2123.
11 Y. Yang, R. Xu, K. Zhang, S.-J. Lee, L. Mu, P. Liu, C. K. Waters, S. Spence, Z. Xu, C. Wei, D. J. Kautz, Q. Yuan, Y. Dong, Y.-S. Yu, X. Xiao, H.-K. Lee, P. Pianetta, P. Cloetens, J.-S. Lee, K. Zhao, F. Lin and Y. Liu, *Adv. Energy Mater.*, 2019, **9**, 1900674.
12 C. Tan, A. S. Leach, T. M. Heenan, H. Parks, R. Jervis, J. N. Weker, D. J. Brett and P. R. Shearing, *Cell Rep. Phys. Sci.*, 2021, **2**, 100647.
13 C. H. Lin, Z. Ju, X. Zheng, X. Zhang, N. Zmich, X. Liu, K. J. Takeuchi, A. C. Marschilok, E. S. Takeuchi, M. Ge, G. Yu and Y. c K. Chen-Wiegart, *Carbon*, 2022, **188**, 114–125.
14 M. Wolf, B. M. May and J. Cabana, *Chem. Mater.*, 2017, **29**, 3347–3362.
15 I. L. Buurmans and B. M. Weckhuysen, *Nat. Chem.*, 2012, **4**, 873–886.
16 S. G. Urquhart, *ACS Omega*, 2022, **7**, 11521–11529.
17 R. Hoppe, J. Reinhardt, G. Hofmann, J. Patommel, J.-D. Grunwaldt, C. D. Damsgaard, G. Wellenreuther, G. Falkenberg and C. G. Schroer, *Appl. Phys. Lett.*, 2013, **102**, 203104.
18 D. A. Shapiro, Y. S. Yu, T. Tyliszczak, J. Cabana, R. Celestre, W. Chao, K. Kaznatcheev, A. L. Kilcoyne, F. Maia, S. Marchesini, Y. S. Meng, T. Warwick, L. L. Yang and H. A. Padmore, *Nat. Photonics*, 2014, **8**, 765–769.
19 Y. S. Yu, M. Farmand, C. Kim, Y. Liu, C. P. Grey, F. C. Strobridge, T. Tyliszczak, R. Celestre, P. Denes, J. Joseph, H. Krishnan, F. R. Maia, A. L. Kilcoyne, S. Marchesini, T. P. C. Leite, T. Warwick, H. Padmore, J. Cabana and D. A. Shapiro, *Nat. Commun.*, 2018, **9**, 1–7.
20 M. Hirose, N. Ishiguro, K. Shimomura, N. Burdet, H. Matsui, M. Tada and Y. Takahashi, *Angew. Chem., Int. Ed.*, 2018, **57**, 1474–1479.
21 M. Hirose, N. Ishiguro, K. Shimomura, D. N. Nguyen, H. Matsui, H. C. Dam, M. Tada and Y. Takahashi, *Commun. Chem.*, 2019, **2**, 1–7.
22 H. Yuan, H. Yuan, T. Casagrande, D. Shapiro, Y. S. Yu, B. Enders, J. R. Lee, A. Van Buuren, M. M. Biener, S. A. Gammon, T. F. Baumann and A. P. Hitchcock, *ACS Appl. Nano Mater.*, 2021, **4**, 621–632.
23 Z. Gao, M. Holler, M. Odstrcil, A. Menzel, M. Guizar-Sicairos and J. Ihli, *Chem. Commun.*, 2020, **56**, 13373–13376.
24 M. Hirose, K. Shimomura, T. Higashino, N. Ishigurob and Y. Takahashia, *J. Synchrotron Radiat.*, 2020, **27**, 455–461.
25 K. Zhang, F. Ren, X. Wang, E. Hu, Y. Xu, X. Q. Yang, H. Li, L. Chen, P. Pianetta, A. Mehta, X. Yu and Y. Liu, *Nano Lett.*, 2017, **17**, 7782–7788.
26 G. Qian, J. Zhang, S. Q. Chu, J. Li, K. Zhang, Q. Yuan, Z. F. Ma, P. Pianetta, L. Li, K. Jung and Y. Liu, *ACS Energy Lett.*, 2021, **6**, 687–693.
27 H. Uematsu, N. Ishiguro, M. Abe, S. Takazawa, J. Kang, E. Hosono, N. D. Nguyen, H. C. Dam, M. Okubo and Y. Takahashi, *J. Phys. Chem. Lett.*, 2021, **12**, 5781–5788.
28 M. Sawamura, S. Kobayakawa, J. Kikkawa, N. Sharma, D. Goonetilleke, A. Rawal, N. Shimada, K. Yamamoto, R. Yamamoto, Y. Zhou, Y. Uchimoto, K. Nakanishi, K. Mitsuhara, K. Ohara, J. Park, H. R. Byon, H. Koga, M. Okoshi, T. Ohta and N. Yabuuchi, *ACS Cent. Sci.*, 2020, **6**, 2326–2338.
29 A. Maiden and J. Rodenburg, *Ultramicroscopy*, 2009, **109**, 1256–1262.
30 M. Hirose, K. Shimomura, N. Burdet and Y. Takahashi, *Opt. Express*, 2017, **25**, 8593.
31 B. Henke, E. Gullikson and J. Davis, *At. Data Nucl. Data Tables*, 1993, **54**, 181–342.
32 K. P. Murphy, *Machine Learning: A Probabilistic Perspective*, The MIT Press, 2012.
33 R. Tibshirani, G. Walther and T. Hastie, *J. Phys. Chem. B*, 2001, **63**, 411–423.
34 P. Chaurand, J. Rose, V. Briois, M. Salome, O. Proux, V. Nassif, L. Olivi, J. Susini, J. L. Hazemann and J. Y. Bottero, *J. Phys. Chem. B*, 2007, **111**, 5101–5110.

35 J. Wong, F. W. Lytle, R. P. Messmer and D. H. Maylotte, *Phys. Rev. B: Condens. Matter Mater. Phys.*, 1984, **30**, 5596–5610.
36 T. Yamamoto, *X-Ray Spectrom.*, 2008, **37**, 572–584.
37 L. de Picciotto, M. Thackeray, W. David, P. Bruce and J. Goodenough, *Mater. Res. Bull.*, 1984, **19**, 1497–1506.
38 E. Salagre, S. Quílez, R. de Benito, M. Jaafar, H. P. van der Meulen, E. Vasco, R. Cid, E. J. Fuller, A. A. Talin, P. Segovia, E. G. Michel and C. Polop, *Sci. Rep.*, 2021, **11**, 1–12.
39 N. Ishiguro and Y. Takahashi, *J. Appl. Crystallogr.*, 2022, **55**, 929–943.

